Check for updates

Received: 16 January 2025 | Revised: 29 April 2025 | Accepted: 2 June 2025

DOI: 10.1002/qj.5039

Quarterly Journal of the Royal Meteorological Society RMetS

RESEARCH ARTICLE

A vertical-slice frontogenesis test case for compressible non-hydrostatic dynamical cores of atmospheric models

Hiroe Yamazaki | **Colin J. Cotter**

Department of Mathematics, Imperial College London, London, UK

Correspondence
Colin J. Cotter, Department of Mathematics, Imperial College London, London, UK.
Email: colin.cotter@imperial.ac.uk

Funding information
Natural Environment Research Council, Grant/Award Number: NE/K012533/1; Engineering and Physical Sciences Research Council, Grant/Award Number: EP/R029628/1

Abstract

A new test case is presented for evaluating the compressible dynamical cores of atmospheric models. The test case is based on a compressible vertical-slice model that can be obtained by simple modification of a standard three-dimensional (3D) compressible dynamical core. On the one hand, an advantage of the test case is that it is quasi-2D, so it can be run quickly on a standard workstation, enabling rapid experimentation with numerical schemes and discretisation choices. On the other hand, the test case exhibits frontogenesis, a challenging regime for numerical discretisations, which usually only arises in 3D model configurations for the compressible case. Numerical results of the test case using an implicit time-stepping method with a compatible finite-element discretisation are presented as a reference solution. An example comparison between advective and vector-invariant forms for the advective nonlinearity in the velocity equation demonstrates one possible use of the scheme. The comparison shows a Hollingsworth-like instability when the vector-invariant form is used.

KEYWORDS

frontogenesis, model intercomparison, numerical weather prediction, vertical slice

1 | INTRODUCTION

Standardised test cases on hierarchies of models are a crucial element of atmospheric model dynamical core development. They are useful for code verification (checking that the code is a correct implementation of the mathematics), evaluation of the quality of discretisation choices (considering, e.g., conservation properties, numerical dissipation and dispersion effects, etc.), benchmarking of computational speed and parallel scalability of models, and general intercomparison of models between modelling groups (Galewsky *et al.*, 2004; Hall *et al.*, 2016; Läuter *et al.*, 2005; Ullrich *et al.*, 2015, 2012, 2017; Williamson *et al.*, 1992; Zarzycki *et al.*, 2019).

Vertical-slice test cases, such as those considered in Melvin *et al.* (2010), are a very useful component of this process, since they can be run quickly on a laptop or workstation, allowing rapid testing and development of numerical schemes, physics parameterisations, data assimilation algorithms, etc. Here we focus on vertical-slice Eady models, which are important because they demonstrate the ability to simulate the geostrophic flows that are the basis

This is an open access article under the terms of the Creative Commons Attribution License, which permits use, distribution and reproduction in any medium, provided the original work is properly cited.
© 2025 The Author(s). *Quarterly Journal of the Royal Meteorological Society* published by John Wiley & Sons Ltd on behalf of Royal Meteorological Society.

of extratropical weather. These models produce fronts that are challenging for numerical models; they are discontinuous and hence they interact with grid-scale numerical stabilisations and closures, but they also set the large-scale balanced flow and hence are coupled to the global solution.

Incompressible Boussinesq vertical-slice Eady models have been in use for several decades (Nakamura, 1994; Visram *et al.*, 2014; Yamazaki *et al.*, 2017). The incompressible Boussinesq equations are not an ideal test for atmospheric models, as they are not a good approximation to the compressible Euler equations, which are used in production atmospheric models, in problems with a significant vertical extent. There is thus a strong desire to reformulate the Eady test case for the compressible equations. Incompressible models rely upon equivalence between the vertical-slice solution and the solution of the three-dimensional (3D) model, but this equivalence cannot be extended to the compressible case. In this work we show that a vertical-slice model formed by the addition of some extra terms to a compressible model has a configuration that causes fronts to form, so that it can be applied to the tasks above. We provide initial conditions and parameter settings that lead to a frontogenesis life cycle similar to the solutions considered in the incompressible case, and we offer this to the modelling community as an additional tool in their evaluation and intercomparison of atmosphere models. In the future, the test case can add further value (as we discuss in Section 4) through comparison with numerical solutions of its semi-geostrophic approximation, as these tools emerge.

In comparison with a full 3D baroclinic wave test case such as that of Ullrich *et al.* (2015), our test case is two-dimensional (2D), so it can feasibly be run on a laptop or workstation, allowing incorporation into an agile design cycle. In common with the 3D test cases, our test case leads to the formation of sharp fronts, where their interaction with numerical stabilisations and closures can be examined. Of course, our 2D geometry does not lead to secondary front instability leading to vortex roll-up: 3D models are necessary for that.

The article is structured as follows. Section 2 presents the full details of the new frontogenesis test case of compressible flow, including the formation of the compressible Eady problem, the settings of the frontogenesis experiment, and the initial conditions. In Section 3, we apply the test case to an example model using an implicit time-stepping method with a compatible finite-element discretisation, to demonstrate front formation.

A summary and outlook is provided in Section 4.

2 | TEST-CASE DESCRIPTION

2.1 | Governing equations

In this section, we describe the model equations that are employed for the new vertical-slice test case for compressible models. In the incompressible case, a 3D Eady problem can be solved using 2D computation by assuming that all variables are independent of y, except for temperature. which has a time-independent linear dependence on y, necessary to support the baroclinic instability that leads to frontogenesis. When compressibility is introduced, it is no longer possible to find similar quasi-2D solutions of the 3D model. We can only introduce ad hoc terms (mimicking the effects of a y-direction temperature gradient) to produce baroclinic instability. This was attempted in Cullen (2008), but unfortunately the proposed modifications did not have a conserved energy or potential vorticity, which are crucial in sustaining baroclinic instability towards frontogenesis. The question of how to build vertical-slice models with conserved energy and potential vorticity was addressed by Cotter and Holm (2013), who identified the variational structure underpinning the incompressible vertical-slice model. This structure establishes energy and potential vorticity conservation from within the vertical-slice setting without needing to refer to the underlying 3D model. Then, other models that also conserve energy and potential vorticity can be derived by choosing a different Lagrangian (kinetic energy minus potential energy). Cotter and Cullen (2019) showed that the potential vorticity conservation in these models arises from a special form of particle relabelling symmetry in the slice geometry that incorporates the velocity in the y-direction. Cotter and Holm (2013) used the variational structure to propose other vertical-slice Eady models, including a compressible model. This zoo was extended to anelastic and pseudocompressible Eady models in Cotter and Holm (2014). When moving away from a linear equation of state, models in this framework are not a reduction of a 3D counterpart, and they serve only to emulate an Eady flow configuration in the vertical-slice setting for the purpose of evaluating numerical models. In the present work, we investigated the compressible vertical-slice Eady model from this framework. It was hoped that energy and potential vorticity conservation would enable sustained baroclinic instability until frontogenesis, and we have indeed found this to be the case. We have made one minor modification to the model proposed by Cotter and Holm (2013), adding a constant perturbation Π_0 to the Exner pressure to reduce the vertical mean horizontal flow, making the setup more suitable for a numerical test problem, since the front is maintained in

1477870x, 2025, 772, Downloaded from https://rmets.onlinelibrary.wiley.com/doi/10.1002/qj.5039 by Imperial College London, Wiley Online Library on [12/03/2026]. See the Terms and Conditions (https://onlinelibrary.wiley.com/terms-and-conditions) on Wiley Online Library for rules of use; OA articles are governed by the applicable Creative Commons License

the same approximate position. This works by adjusting the geostrophic balanced x-component of the flow that is set in Equation (2) below when the advective terms are neglected.

The equations are

$$\frac{\partial \boldsymbol{u}}{\partial t} + (\boldsymbol{u}\cdot\nabla)\boldsymbol{u} - fv\,\hat{\boldsymbol{x}} = -c_\mathrm{p}\theta_S\nabla\Pi - g\hat{\boldsymbol{z}}, \tag{1}$$

$$\frac{\partial v}{\partial t} + (\boldsymbol{u}\cdot\nabla)v + f\boldsymbol{u}\cdot\hat{\boldsymbol{x}} = \underbrace{c_\mathrm{p}s(\Pi-\Pi_0)}_{\text{extra}}, \tag{2}$$

$$\frac{\partial \theta_S}{\partial t} + (\boldsymbol{u}\cdot\nabla)\theta_S = \underbrace{-vs}_{\text{extra}}, \tag{3}$$

$$\frac{\partial D}{\partial t} + \nabla\cdot(D\boldsymbol{u}) = 0, \tag{4}$$

where $\boldsymbol{u} = (u, w)$ is the velocity vector in the vertical slice, $\nabla = (\partial_x, \partial_z)$ is the gradient operator in the vertical slice, v is the out-of-slice velocity component, $\hat{\boldsymbol{x}}$ is a unit vector in the x-direction and $\hat{\boldsymbol{z}}$ that in the z-direction; D is the density, θ is the potential temperature, f is the rotation frequency, g is the acceleration due to gravity, and θ_S is a "perturbation potential temperature", with the idea that the total potential temperature $\theta \approx sy + \theta_S$ in the region near $y = 0$ where the slice model is defined. For scaling purposes, we write

$$s = -\frac{\theta_0 f\Lambda}{g} = \text{const.}, \tag{5}$$

where θ_0 is a reference density at the surface and Λ is the constant vertical shear. Further, the Exner pressure Π depends on θ_S and D such that

$$\Pi = \left(\frac{p}{p_0}\right)^{R/c_\mathrm{p}}, \qquad p = DR\underbrace{T}_{=\theta_S\Pi}, \tag{6}$$

where p is the pressure, p_0 is a reference pressure, $R = c_\mathrm{p} - c_\mathrm{v}$ is the specific gas constant, c_p is the specific heat at constant pressure, and c_v is the specific heat at constant volume. All the variables $\boldsymbol{u}$, v, θ_S, D, and Π depend on (x, z, t) only, hence the model can be solved on a 2D mesh.

It is important to note here that it is not physically correct to have Π depending on θ_S rather than θ, but this modification is necessary to have a well-defined vertical-slice model. This model is not intended to predict physical phenomena skilfully, but rather to provide a challenging test case for atmosphere model numerics in a 2D configuration. This configuration can also be obtained by setting periodic boundary conditions in a 3D model (in local area model mesh configuration) in the y-direction and then making the mesh only one element wide (which is what we did in this article). This is then testing the same code that is used in the 3D model, which is useful for verification purposes; it is also potentially more achievable in a code framework that does not switch easily between 3D and 2D. After this is done, the only other required changes to a 3D model are to insert the terms indicated as "extra" in Equations (1–4), having identified θ in the 3D model with θ_S in the vertical-slice model.

The vertical-slice model has steady-state solutions when θ_S depends on z only, with $v = 0$, Π obtained from the hydrostatic balance:

$$0 = -c_\mathrm{p}\theta_S\frac{\partial\Pi}{\partial z} - g, \tag{7}$$

and u obtained from the geostrophic balance:

$$fu = c_\mathrm{p}s(\Pi - \Pi_0). \tag{8}$$

This solution can only be sustained with periodic boundary conditions in the x-direction. Here we see the role of Π_0: without it, the vertical mean of u will be large and everything will propagate rapidly to the right.

This modification has a conserved total energy $E = K_u + K_v + P$, given by

$$K_u = \frac{1}{2}\int_\Omega D|\boldsymbol{u}|^2 \; dx\,dz, \tag{9}$$

$$K_v = \frac{1}{2}\int_\Omega Dv^2 \; dx\,dz, \tag{10}$$

$$P = \int_\Omega D\left(gz + c_\mathrm{v}\Pi\theta - c_\mathrm{p}\Pi_0\theta\right) \; dx\,dz, \tag{11}$$

where K_u is the kinetic energy from the in-slice velocity components, K_v is the kinetic energy from the out-of-slice velocity component, and P is the potential energy, comprising contributions from gravitational potential energy and internal energy. For further discussion of the energy conservation and potential vorticity, see Appendix A.

2.2 | Experimental settings

2.2.1 | Constants

In the frontogenesis experiments, the model constants are set to the values below, following the incompressible Euler–Boussinesq Eady test case (e.g., Cullen, 2007; Nakamura, 1994; Visram, 2014; Visram *et al.*, 2014; Yamazaki *et al.*, 2017):

$$\begin{aligned} &L = 1000\ \text{km}, && H = 10\ \text{km}, && f = 10^{-4}\ \text{s}^{-1},\\ &g = 10\ \text{m}\cdot\text{s}^{-2}, && p_0 = 10^5\ \text{Pa}, && \theta_0 = 300\ \text{K},\\ &\Lambda = 10^{-3}\ \text{s}^{-1}, && N^2 = 2.5\times10^{-5}\ \text{s}^{-1}, && \Pi_0 = 0.864, \end{aligned} \tag{12}$$

1477870x, 2025, 772, Downloaded from https://rmets.onlinelibrary.wiley.com/doi/10.1002/qj.5039 by Imperial College London, Wiley Online Library on [12/03/2026]. See the Terms and Conditions (https://onlinelibrary.wiley.com/terms-and-conditions) on Wiley Online Library for rules of use; OA articles are governed by the applicable Creative Commons License

where L and H determine the model domain $\Omega = [-L, L] \times [0, H]$ and N is the Brunt–Väisälä frequency. The y derivative, s, of the background temperature in Equations (3) and (2) is therefore calculated as $s = -3.0 \times 10^{-6}$. The corresponding Rossby and Froude numbers are $\mathrm{Ro} = u_0/fL = 0.05$, $\mathrm{Fr} = u_0/NH = 0.1$, where $u_0 = 5\ \mathrm{m \cdot s^{-1}}$ is used as a representative velocity (estimated from the unperturbed background state). The ratio of the Rossby number to the Froude number defines the Burger number, $\mathrm{Bu} = \mathrm{Ro}/\mathrm{Fr} = 0.5$, which is used in the next section for initialising the model.

2.2.2 | Initialisation

The model field is initialised with a small perturbation to a balanced steady state. The steady-state temperature is isothermal,

$$\bar{\theta}(z) = \theta_0 \exp[N^2(z - H/2)/g]. \tag{13}$$

Then, following the incompressible Euler–Boussinesq Eady test case (e.g., Cullen, 2007; Nakamura, 1994; Visram *et al.*, 2014; Yamazaki *et al.*, 2017), a small perturbation is applied to the in-slice temperature,

$$\theta_S(x,z) = \bar{\theta} + \frac{\theta_0 a N}{g}\left\{-\left[1 - \frac{\mathrm{Bu}}{2}\coth\left(\frac{\mathrm{Bu}}{2}\right)\right]\right. \\ \left.\sinh Z \cos\left(\frac{\pi x}{L}\right) - n\ \mathrm{Bu}\cosh Z \sin\left(\frac{\pi x}{L}\right)\right\}, \tag{14}$$

which is the structure of the normal mode taken from Williams (1967). The constant a corresponds to the amplitude of the perturbation and the constant n takes the form

$$n = \frac{1}{\mathrm{Bu}}\left\{\left[\frac{\mathrm{Bu}}{2} - \tanh\left(\frac{\mathrm{Bu}}{2}\right)\right]\left[\coth\left(\frac{\mathrm{Bu}}{2}\right) - \frac{\mathrm{Bu}}{2}\right]\right\}^{1/2}. \tag{15}$$

The modified vertical coordinate Z is defined as

$$Z = \mathrm{Bu}\left[\left(\frac{z}{H}\right) - \frac{1}{2}\right]. \tag{16}$$

In fact, this is not a normal mode of the linearisation of the compressible vertical-slice model. Instead, we rely upon initialising a balanced initial condition, which will trigger a balanced baroclinically unstable mode. This is why our experiment has an initial growth period before resetting the clock to 0 when the amplitude starts to become visible.

Next we initialise the density D. Given the initial temperature θ_S in Equation (14), first we seek Π in hydrostatic balance,

$$c_\mathrm{p}\theta_S\frac{\partial \Pi}{\partial z} = -g. \tag{17}$$

Once we have the profile of the initial Π, we can calculate the initial density by using Equation (6) as

$$D = \frac{p_0 \Pi^{c_\mathrm{v}/R_\mathrm{d}}}{R_\mathrm{d}\theta_0}. \tag{18}$$

Alternatively, we can solve the nonlinear problem of finding D such that Equation (17) holds, treating Π as the prescribed function of D and θ_S given in Equation (6). This is what we did in our experiments (see Cotter & Shipton, 2023 for details).

Then we initialise the out-of-slice velocity v by seeking a velocity in geostrophic balance with the initialised θ_S and Π:

$$-fv = -c_\mathrm{p}\theta_S\frac{\partial \Pi}{\partial x}. \tag{19}$$

Finally, we initialise the in-slice velocity u according to

$$u = \frac{c_\mathrm{p}}{f}\frac{\partial \bar{\theta}}{\partial y}(\Pi - \Pi_0). \tag{20}$$

Here Π_0 was chosen following numerical experiments to minimise the horizontal drift of the front structures once they have formed.

In addition to the initialisation of the model field described above, we introduce a breeding procedure at the beginning of each simulation to remove any remaining unbalanced modes in the initial condition, as in Visram *et al.* (2014), Visram *et al.* (2014), and Yamazaki *et al.* (2017). In the experiments performed in Section 3, the model field is initialised with a small perturbation by choosing $a = -7.5$ in Equation (14), following the previous studies. Figure 1 shows the initial conditions of density D, potential temperature θ, and out-of-slice velocity v. The simulation is then advanced until the maximum amplitude of v reaches $3\ \mathrm{m \cdot s^{-1}}$, at which point the time is reset to zero to match the amplitude of the initial perturbation with that of the incompressible Euler–Boussinesq Eady models (Nakamura & Held, 1989; Visram *et al.*, 2014; Yamazaki *et al.*, 2017) as closely as possible. In the results presented in Section 3, the time is reset to zero after 50 hours.

3 | RESULTS

In this section, we present the results of the frontogenesis experiments using the new test case developed in

1477870x, 2025, 772, Downloaded from https://rmets.onlinelibrary.wiley.com/doi/10.1002/qj.5039 by Imperial College London, Wiley Online Library on [12/03/2026]. See the Terms and Conditions (https://onlinelibrary.wiley.com/terms-and-conditions) on Wiley Online Library for rules of use; OA articles are governed by the applicable Creative Commons License

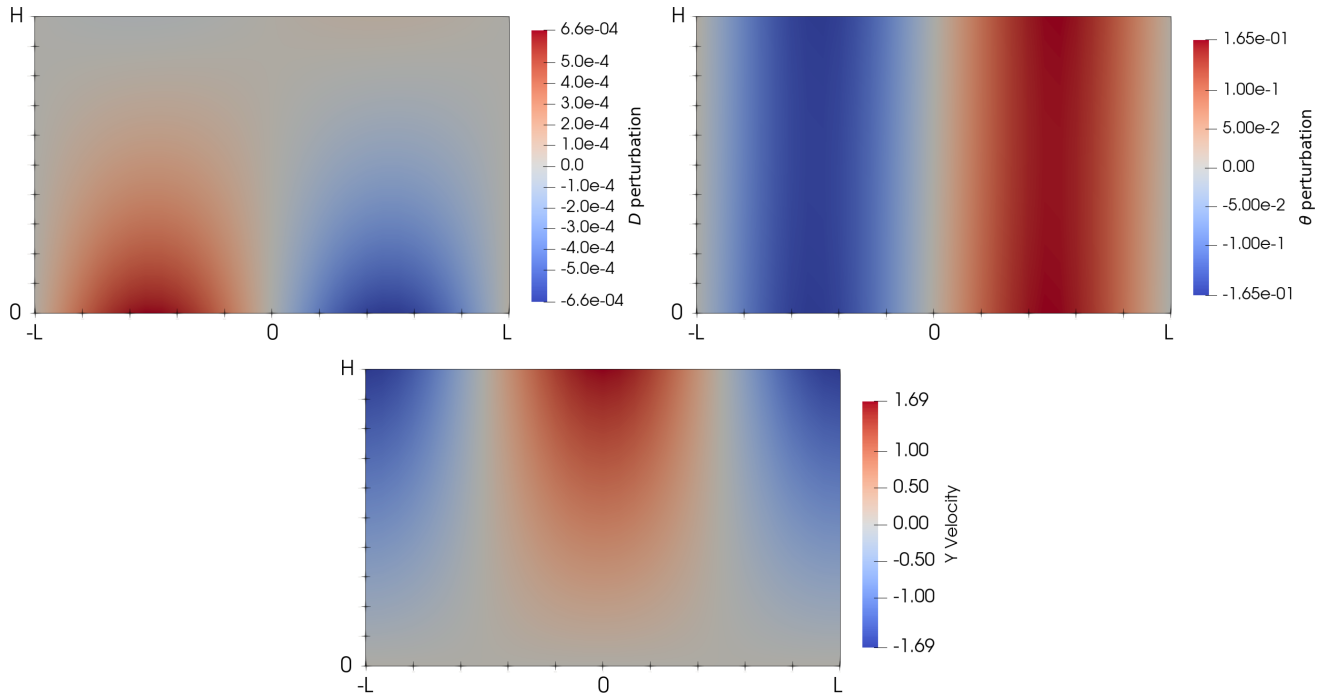


FIGURE 1 Initial conditions of density D (top left), potential temperature θ (top right), and out-of-slice velocity v (bottom) in the experiments performed in Section 3. Note that density and temperature are shown here as differences from a reference value.

this study, with the use of the finite-element code generation library Firedrake (Ham *et al.*, 2023). Since this article is about the test case and not the specific numerical discretisation, we just mention briefly that we used a compatible finite-element discretisation following Cotter and Shipton (2023) in 3D configuration on a mesh that is one cell wide and periodic in the y-direction, with two differences. First, we did not use the edge stabilisation recommended there for θ_S transport, as it led to instabilities after the front formed, requiring further investigation. It appears that the horizontal discontinuous Galerkin upwinding for θ_S is sufficient for this problem, probably because the curvature of the solution is mainly in the horizontal direction. Second, we did not use a vector-invariant form of the velocity advection equation, instead using a discretisation of the standard advective form $(\boldsymbol{u}\cdot\nabla)\boldsymbol{u}$ in our main results, using the upwind formulation of Cockburn *et al.* (2007) for that term instead. This is discussed more later. The time-stepping method is the implicit midpoint rule, which is solved using Newton's method and generalised minimal residual preconditioned by the column-patch additive Schwarz method, which is also described in Cotter and Shipton (2023). This scheme is unconditionally stable and preserves energy for linear wave equations; any dissipation in the model is coming from upwinding in the spatial discretisation.

The constants used to set up the experiments are shown in Section 2.2.1. At the beginning of each experiment, the model is initialised in the way described in Section 2.2.2, then integrated for 25 days in each experiment.

In our solution, the model resolution is given by

$$\Delta x = \frac{2L}{N}, \qquad \Delta z = \frac{H}{N}, \tag{21}$$

where N is the number of quadrilateral elements in the x- and z-directions. Unless stated otherwise, we use a resolution of $N = 30$ and the time step Δt of 300 s as a control run.

Figures 2a and 3a show the snapshots of the out-of-slice velocity v and potential temperature θ fields, respectively. At day 2, both fields show very similar structures to those from the simulation using the linearised equations in Visram *et al.* (2014). The model shows some early signs of front formation at day 4. The frontal discontinuity becomes most intense around day 7. At day 11, the vertical tilt in the v-field reverses, which is a sign of energy conversion from kinetic back to potential energy. Overall, these results are consistent with the incompressible Eady models (Cullen, 2007; Nakamura & Held, 1989; Visram, 2014; Visram *et al.*, 2014; Yamazaki *et al.*, 2017). The black curve in Figure 4a shows the time evolution of the root-mean-square of v (RMSV) in our model. The result shows that the model reproduces several further quasi-periodic life cycles after the first frontogenesis.

To evaluate the effect of resolution on our model result, we repeated the experiment using $N = 60$, 90, and 120

1477870x, 2025, 772, Downloaded from https://rmets.onlinelibrary.wiley.com/doi/10.1002/qj.5039 by Imperial College London, Wiley Online Library on [12/03/2026]. See the Terms and Conditions (https://onlinelibrary.wiley.com/terms-and-conditions) on Wiley Online Library for rules of use; OA articles are governed by the applicable Creative Commons License

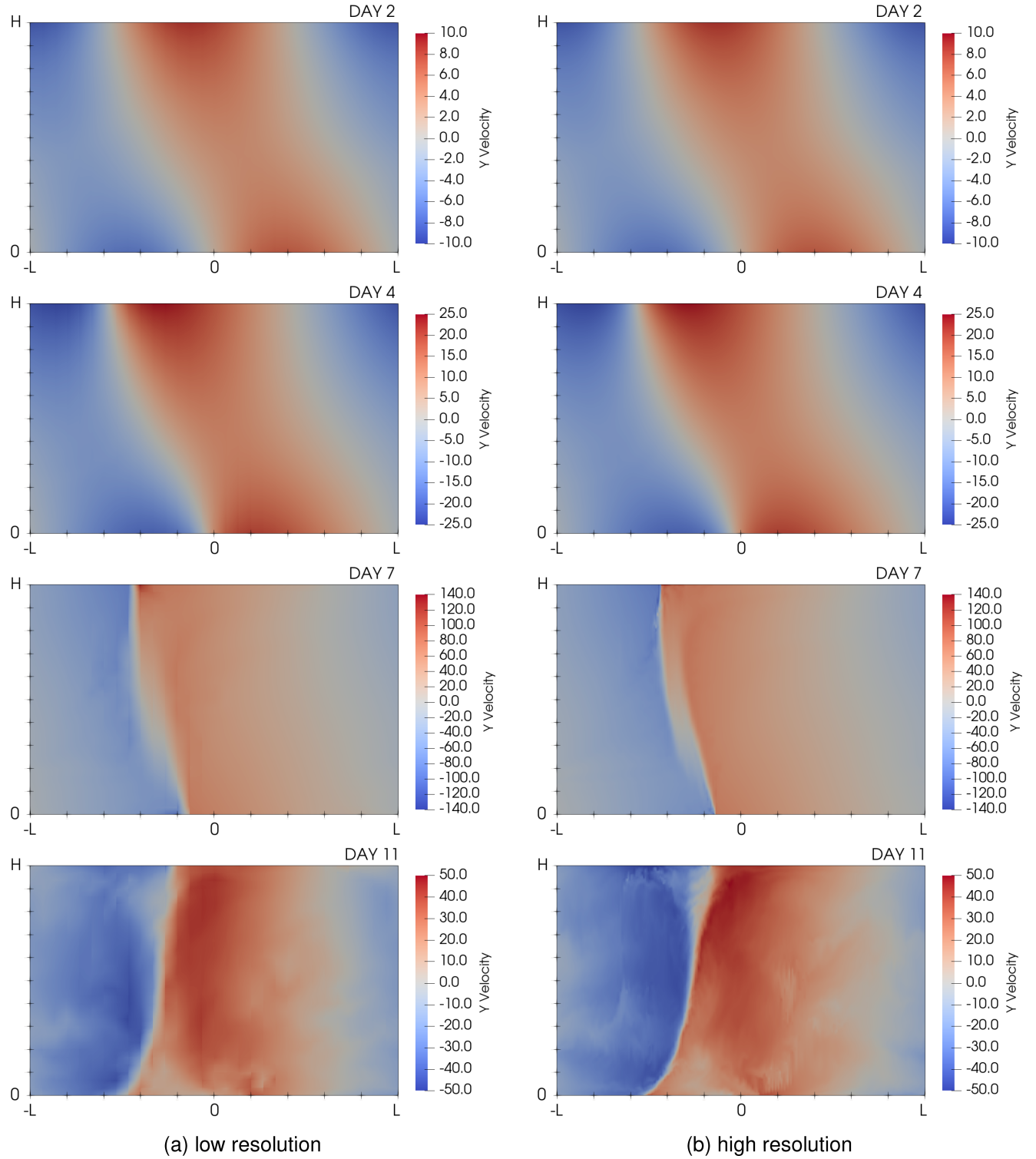


FIGURE 2 Snapshots of out-of-slice velocity fields at days 2, 4, 7, and 11 in (a) the control run at $N = 30$ and (b) the highest resolution run at $N = 120$.

with time steps of $\Delta t = 150$, 100, and 75 s, respectively. The snapshots of the out-of-slice velocity v and potential temperature θ fields in the highest resolution run using $N = 120$ are shown in Figures 2b and 3b, respectively. Although the results look similar to that of the control run in the early days, sharper fronts are formed at days 7 and 11. The evolution of RMSV in the high-resolution runs is shown by the coloured curves in Figure 4a. The higher the resolution, the bigger the RMSV observed at the peaks. Figure 4b shows the enlarged picture around the first peak of the RMSV in Figure 4a. We can see that the peak RMSV is converging as we increase the resolution. Table 1 shows

1477870x, 2025, 772, Downloaded from https://rmets.onlinelibrary.wiley.com/doi/10.1002/qj.5039 by Imperial College London, Wiley Online Library on [12/03/2026]. See the Terms and Conditions (https://onlinelibrary.wiley.com/terms-and-conditions) on Wiley Online Library for rules of use; OA articles are governed by the applicable Creative Commons License

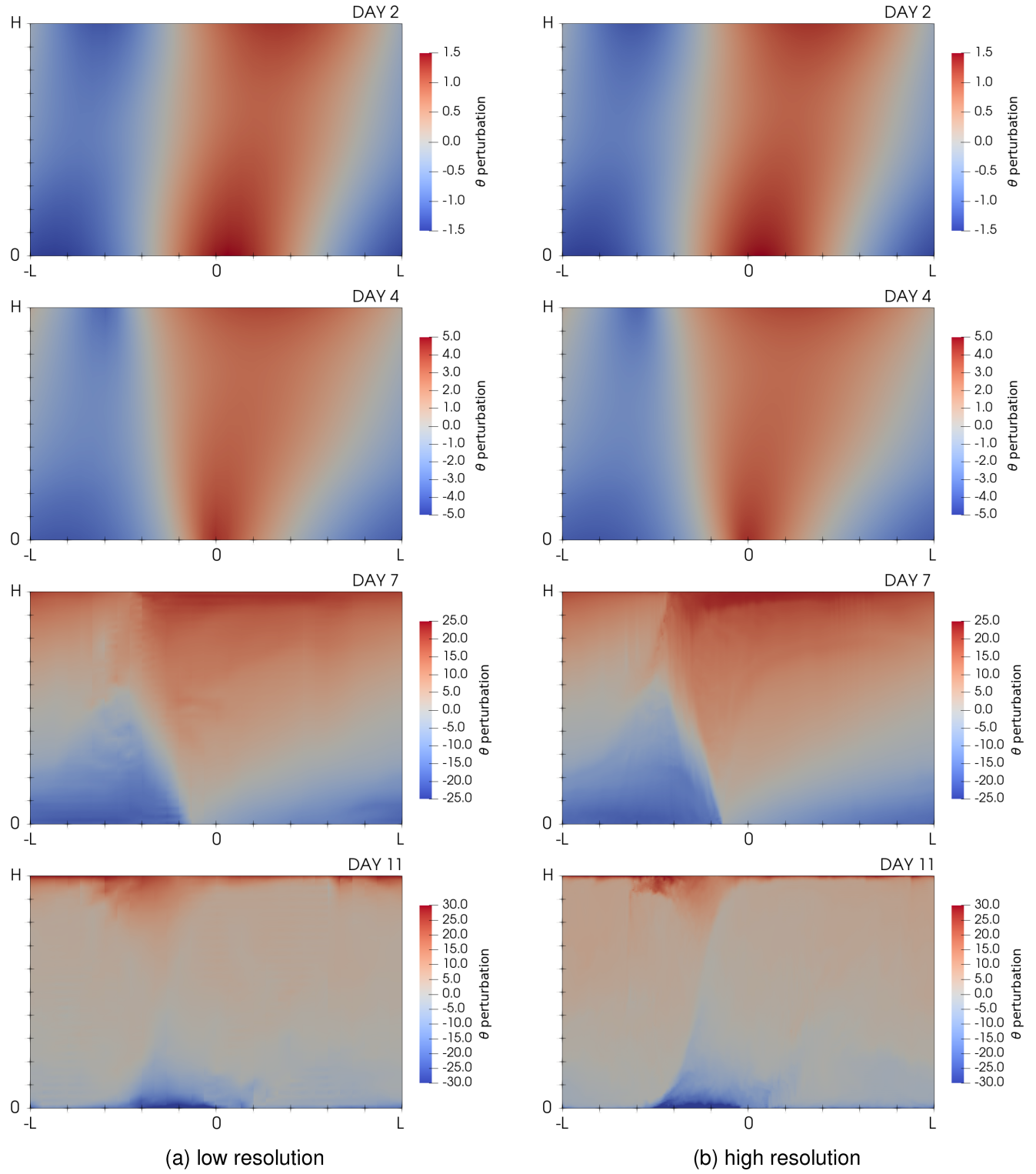


FIGURE 3 Snapshots of in-slice temperature perturbation field at days 2, 4, 7, and 11 in (a) the control run at $N = 30$ and (b) the highest resolution run at $N = 120$.

the time and value of the peak RMS v value, indicating the moment of maximum front strength. This value is a useful bulk quantity to use for comparing different models and schemes. Figure 5 plots the differences in the peak maximum amplitudes of v at N =30, 60, and 90 from that in the highest resolution run at $N = 120$. We can see that the peak amplitude converges as we increase the resolution. Figure 6 shows the L_2 norms of the global errors in the potential temperature and velocity by assuming the solution with the highest resolution of $N = 120$ as the exact

1477870x, 2025, 772, Downloaded from https://rmets.onlinelibrary.wiley.com/doi/10.1002/qj.5039 by Imperial College London, Wiley Online Library on [12/03/2026]. See the Terms and Conditions (https://onlinelibrary.wiley.com/terms-and-conditions) on Wiley Online Library for rules of use; OA articles are governed by the applicable Creative Commons License

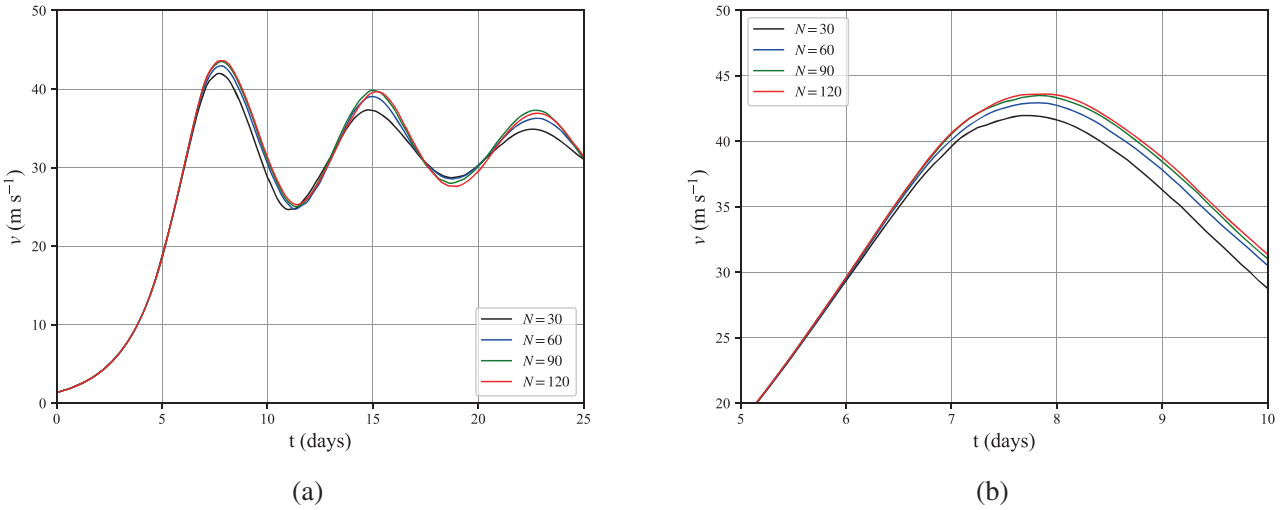


FIGURE 4 The root-mean-square of the out-of-slice velocity v when using $N = 30$ (black), $N = 60$ (blue), $N = 90$ (green), and $N = 120$ (red). (b) shows the enlarged view of (a) around the first peak.

TABLE 1 Table showing the time and peak value of the RMS value of v, for intercomparison. This time indicates when the front is at its strongest.

N	t (s)	v (m · s^{-1})
30	672,600	41.99
60	677,550	42.95
90	675,800	43.51
120	681,900	43.61

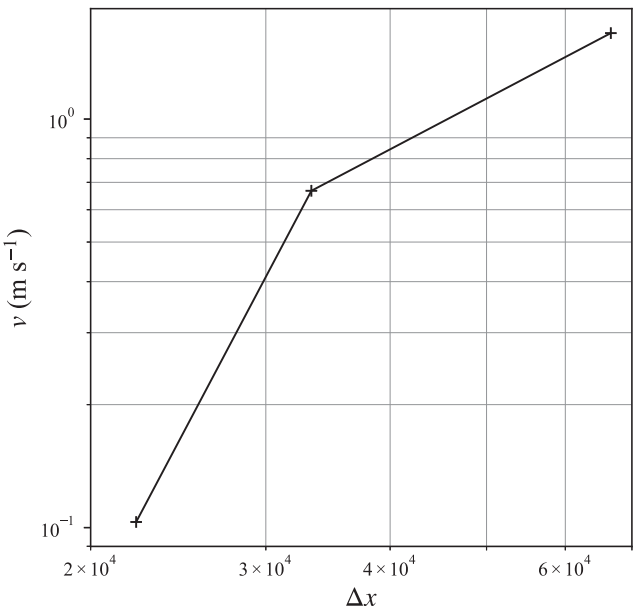


FIGURE 5 The difference of the peak maximum amplitude of the out-of-slice velocity v when using $N = 30$, 60, and 90 from that using $N = 120$. The values are calculated from the numbers listed in Table 1.

solution. The global error decreases as we increase the resolution, with slower convergence when the front forms due to strong discontinuities.

Figure 7 shows the time evolution of the total energy E, kinetic energy K_u and K_v, and potential energy P, which are defined by Equations (9–11). We observe a loss of energy after the front is formed, which is due to loss of available potential energy caused by numerical dissipation in the θ_S equation as well as loss of K_v due to numerical dissipation in the v equation. This demonstrates the challenge posed by fronts in atmosphere models; numerical dissipation is necessary to stabilise advection in the model, but also alters the large-scale circulation.

Finally, as an example of how the test case might be used to compare numerical schemes, we replace the advection term $(\boldsymbol{u} \cdot \nabla)\boldsymbol{u}$ in the velocity equation with the vector-invariant form $(\nabla \times \boldsymbol{u}) \times \boldsymbol{u} + |\boldsymbol{u}|^2/2$, using the upwind discretisation of Cotter and Shipton (2023). As shown in Figure 8, by day 6 the version using the vector-invariant form has developed oscillations that are polluting the solution. We believe that this is related to the "Hollingsworth instability", which is much discussed in the dynamical core literature (Bell *et al.*, 2017; Gassmann, 2013; Hollingsworth *et al.*, 1983; Lazić *et al.*, 1984; Peixoto *et al.*, 2018). This example requires further investigation, but might provide a useful laboratory for understanding further how to control that instability.

4 | SUMMARY AND OUTLOOK

A new vertical-slice test case is developed for compressible non-hydrostatic dynamical cores of atmospheric models,

1477870x, 2025, 772, Downloaded from https://rmets.onlinelibrary.wiley.com/doi/10.1002/qj.5039 by Imperial College London, Wiley Online Library on [12/03/2026]. See the Terms and Conditions (https://onlinelibrary.wiley.com/terms-and-conditions) on Wiley Online Library for rules of use; OA articles are governed by the applicable Creative Commons License

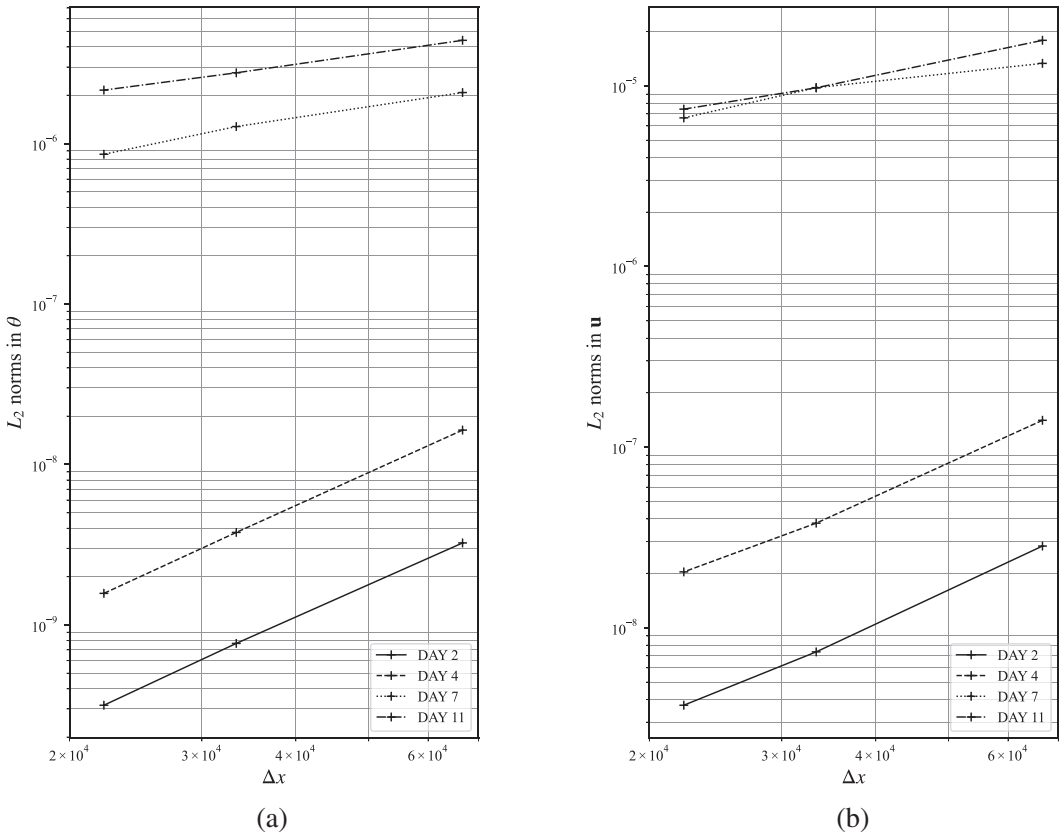
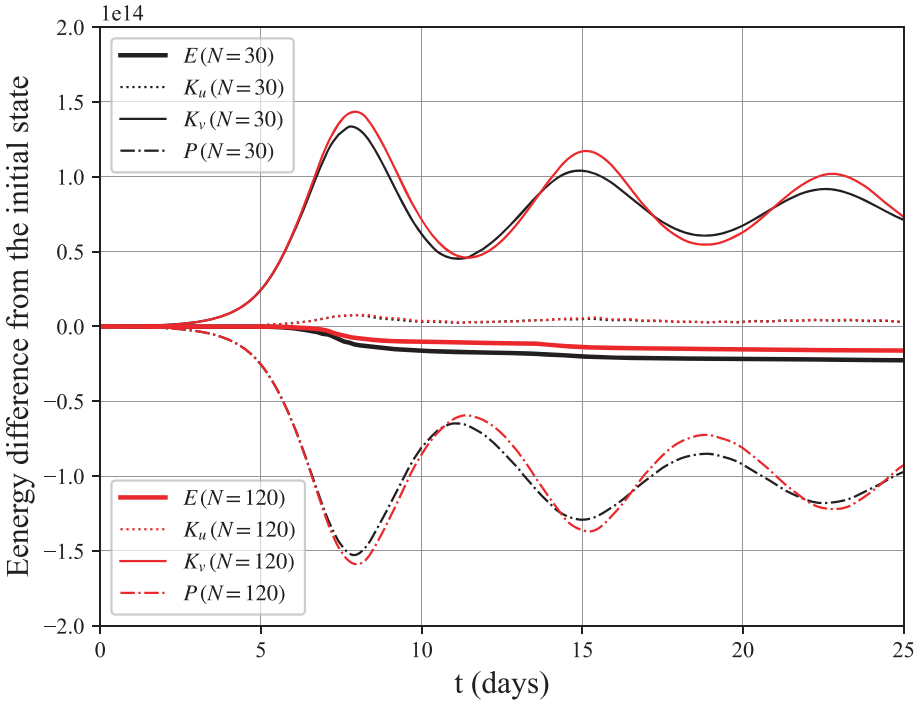


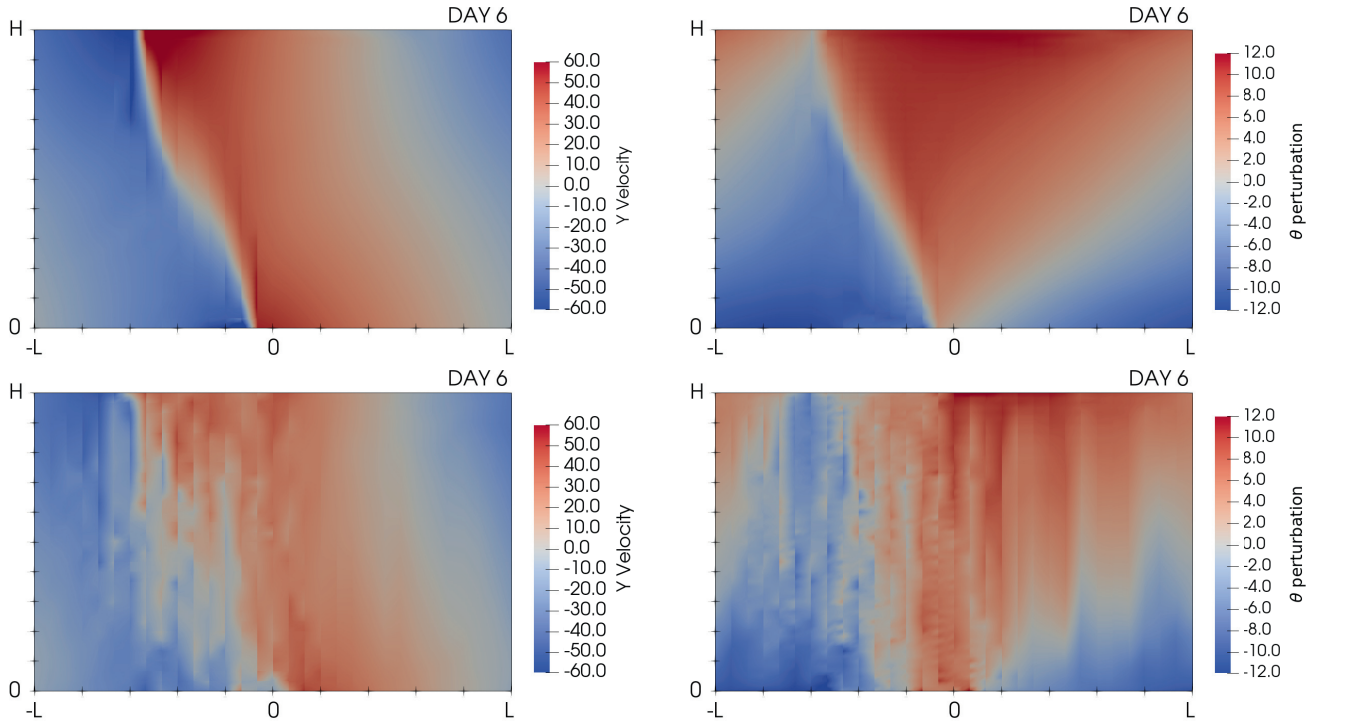
FIGURE 6 Variation of L_2 norms of the global error in (a) θ and (b) $\boldsymbol{u}$ with the grid interval in the x-direction.

FIGURE 7 Time evolution of energy when using $N = 30$ (black) and $N = 120$ (red). The thick line represents the evolution of total energy. Dotted and solid lines represent the evolution of in-slice and out-of-slice components of the kinetic energy. The dot–dashed line represents the evolution of potential energy.



and solutions of a model using an implicit time-stepping method and a compatible finite-element method were presented as a reference. The test case can be run by adding two terms to a 3D atmosphere model in local area mode, that is, a Cartesian box with periodicity and which is one cell wide in the y-direction. It provides the capability to

1477870x, 2025, 772, Downloaded from https://rmets.onlinelibrary.wiley.com/doi/10.1002/qj.5039 by Imperial College London, Wiley Online Library on [12/03/2026]. See the Terms and Conditions (https://onlinelibrary.wiley.com/terms-and-conditions) on Wiley Online Library for rules of use; OA articles are governed by the applicable Creative Commons License



(a) Out-of-slice velocity field

(b) In-slice temperature perturbation field

FIGURE 8 Snapshots of out-of-slice velocity and in-slice temperature perturbation at day 6. Top: advective form, bottom: vector-invariant form. (a) Out-of-slice velocity field, (b) in-slice temperature perturbation field.

explore the behaviour of discretisations in the presence of challenging fronts, but in a quasi-2D configuration that allows rapid turnaround for numerical experiments. The equations for the test case do not correspond to the reduction of a 3D model to a 2D vertical-slice configuration, since this is not possible for a compressible model with nonlinear equation of state. However, it serves our purpose, since we observe solutions that produce features characteristic of atmospheric fronts, with which we would like to challenge our numerical schemes.

We demonstrated that the test case produces quasi-periodic life cycles of fronts, which are observed despite the presence of strong discontinuities; these are sustained because the equations have conserved energy and potential vorticity. Without this formulation, solutions are insufficiently constrained to drive strong fronts, as was observed by Cullen (2008). The general results of frontogenesis are consistent with results from the incompressible Euler–Boussinesq models, so we have been successful in our goals for the test case.

We hope that this test case becomes adopted by atmosphere modelling groups, allowing intercomparisons of different discretisations and approaches. One possible use for the test case is to understand how subgrid schemes, both explicit and implicit, behave in the region of fronts. For example, the compressible version of the α-Euler vertical-slice model of Cotter and Holm (2013) could be used for this. In addition, the test case could be extended to include the effects of moisture and boundary-layer physics, for example.

Ideally, we would like to use test cases to develop confidence that the numerical solutions are converging to the true solution, but error calculations require a known exact solution. Exact solutions of the nonlinear equations are hard to find, especially solutions that are relevant to specific types of atmospheric flow. As an alternative, Cullen (2007) proposed considering asymptotic limits (such as the quasi-geostrophic or semi-geostrophic limit), demonstrating convergence in the asymptotic limit to numerical solutions of the limit equation where the error is more under control.

Here we focus on the vertical-slice Eady problem, which is important because it demonstrates the ability to simulate the geostrophic flows that are the basis of extra-tropical weather. In the incompressible Boussinesq case, the Euler solutions can be shown formally to converge to the solutions of the simpler semi-geostrophic system as a scaling parameter tends to zero. The latter solutions are discontinuous, and can be computed rigorously to any desired accuracy by optimal transport methods (Benamou *et al.*, 2024; Cullen, 2006; Egan *et al.*, 2022; Lavier, 2024). They thus provide a challenging test for numerical

1477870x, 2025, 772, Downloaded from https://rmets.onlinelibrary.wiley.com/doi/10.1002/qj.5039 by Imperial College London, Wiley Online Library on [12/03/2026]. See the Terms and Conditions (https://onlinelibrary.wiley.com/terms-and-conditions) on Wiley Online Library for rules of use; OA articles are governed by the applicable Creative Commons License

methods for the Euler equations. Further, considering Euler, any solution will require regularisation, and Nakamura (1994) showed strong sensitivity to the choice of regularisation. The semi-geostrophic limit solution is well defined and conserves energy, with no need for regularisation. Hence, it can be argued that the correct limiting solution for Euler should have minimal numerical regularisation (explicit or implicit). For the incompressible vertical-slice Eady model in the semi-geostrophic limit, the asymptotic limit programme was pursued by Visram *et al.* (2014) and Yamazaki *et al.* (2017).

The incompressible Boussinesq equations are not an ideal test for atmospheric models, as they are not a good approximation to the compressible Euler equations, which are used in production atmospheric models, in problems with a significant vertical extent. There is thus a strong desire to reformulate the Eady test case for the compressible equations.

To complete the programme of Cullen (2007) in this setting, it remains to prove rigorously that the solution of our compressible vertical-slice model converges in the semi-geostrophic limit to solutions of their semi-geostrophic counterpart, following an adaptation of Cullen and Maroofi (2003) to include the extra terms marked in Equations (1–4). We leave this mathematical analysis to future work. This framework can also be used to obtain a numerical semi-geostrophic reference solution, following the approaches of Egan *et al.* (2022) and Benamou *et al.* (2024). The extension of these approaches to the compressible setting is the subject of ongoing work, for which the existence of the test case in this article is extremely useful.

ACKNOWLEDGEMENTS

We are grateful for funding from EPSRC via grant EP/R029628/1, and from NERC via grant NE/K012533/1. We thank Thomas Bendall, Mike Cullen, Darryl Holm, and Jemma Shipton for their helpful comments on our article. Any errors are the authors' own.

DATA AVAILABILITY STATEMENT

There are no data associated with this work.

ORCID

Colin J. Cotter https://orcid.org/0000-0001-7962-8324

REFERENCES

Bell, M.J., Peixoto, P.S. & Thuburn, J. (2017) Numerical instabilities of vector-invariant momentum equations on rectangular C-grids. *Quarterly Journal of the Royal Meteorological Society*, 143(702), 563–581.

Benamou, J.-D., Cotter, C.J. & Malamut, H. (2024) Entropic optimal transport solutions of the semigeostrophic equations. *Journal of Computational Physics*, 500, 112745.

Cockburn, B., Kanschat, G. & Schötzau, D. (2007) A note on discontinuous Galerkin divergence-free solutions of the Navier–Stokes equations. *Journal of Scientific Computing*, 31, 61–73.

Cotter, C.J. & Cullen, M. (2019) Particle relabelling symmetries and Noether's theorem for vertical slice models. *Journal of Geometric Mechanics*, 11(2), 139–151.

Cotter, C. & Holm, D. (2013) A variational formulation of vertical slice models. *Proceedings of the Royal Society A: Mathematical, Physical and Engineering Sciences*, 469(2155), 20120678.

Cotter, C. & Holm, D. (2014) Variational formulations of sound-proof models. *Quarterly Journal of the Royal Meteorological Society*, 140(683), 1966–1973.

Cotter, C.J. & Shipton, J. (2023) A compatible finite element discretisation for the nonhydrostatic vertical slice equations. *GEM-International Journal on Geomathematics*, 14(1), 25.

Cullen, M.J. (2006) *A mathematical theory of large-scale atmosphere/ocean flow*. London: Imperial College Press.

Cullen, M. (2007) Modelling atmospheric flows. *Acta Numerica*, 16, 67–154.

Cullen, M. (2008) A comparison of numerical solutions to the Eady frontogenesis problem. *Quarterly Journal of the Royal Meteorological Society*, 134(637), 2143–2155.

Cullen, M. & Maroofi, H. (2003) The fully compressible semi-geostrophic system from meteorology. *Archive for Rational Mechanics and Analysis*, 167, 309–336.

Egan, C.P., Bourne, D.P., Cotter, C.J., Cullen, M.J., Pelloni, B., Roper, S.M. et al. (2022) A new implementation of the geometric method for solving the Eady slice equations. *Journal of Computational Physics*, 469, 111542.

Galewsky, J., Scott, R.K. & Polvani, L.M. (2004) An initial-value problem for testing numerical models of the global shallow-water equations. *Tellus A: Dynamic Meteorology and Oceanography*, 56(5), 429–440.

Gassmann, A. (2013) A global hexagonal C-grid non-hydrostatic dynamical core (ICON-IAP) designed for energetic consistency. *Quarterly Journal of the Royal Meteorological Society*, 139(670), 152–175.

Hall, D.M., Ullrich, P.A., Reed, K.A., Jablonowski, C., Nair, R.D. & Tufo, H.M. (2016) Dynamical Core Model Intercomparison Project (DCMIP) tracer transport test results for CAM-SE. *Quarterly Journal of the Royal Meteorological Society*, 142(697), 1672–1684.

Ham, D.A., Kelly, P.H.J., Mitchell, L., Cotter, C.J., Kirby, R.C., Sagiyama, K. et al. (2023) Firedrake User Manual. Imperial College London and University of Oxford and Baylor University and University of Washington, first edition Edition.

Hollingsworth, A., Kållberg, P., Renner, V. & Burridge, D. (1983) An internal symmetric computational instability. *Quarterly Journal of the Royal Meteorological Society*, 109(460), 417–428.

Läuter, M., Handorf, D. & Dethloff, K. (2005) Unsteady analytical solutions of the spherical shallow water equations. *Journal of Computational Physics*, 210(2), 535–553.

Lavier, T. (2024) A semi-discrete optimal transport scheme for the 3d incompressible semi-geostrophic equations. arXiv preprint arXiv:2411.00575.

Lazić, L., Janjić, Z. & Mesinger, F. (1984) non-cancellation instability in horizontal advection schemes for momentum equations. *Meteorology and Atmospheric Physics*, 35(1), 49–52.

1477870x, 2025, 772, Downloaded from https://rmets.onlinelibrary.wiley.com/doi/10.1002/qj.5039 by Imperial College London, Wiley Online Library on [12/03/2026]. See the Terms and Conditions (https://onlinelibrary.wiley.com/terms-and-conditions) on Wiley Online Library for rules of use; OA articles are governed by the applicable Creative Commons License

Melvin, T., Dubal, M., Wood, N., Staniforth, A. & Zerroukat, M. (2010) An inherently mass-conserving iterative semi-implicit semi-Lagrangian discretization of the non-hydrostatic vertical-slice equations. *Quarterly Journal of the Royal Meteorological Society*, 136(648), 799–814.

Nakamura, N. (1994) Nonlinear equilibration of two-dimensional Eady waves: simulations with viscous geostrophic momentum equations. *Journal of the Atmospheric Sciences*, 51(7), 1023–1035.

Nakamura, N. & Held, I.M. (1989) Nonlinear equilibration of two-dimensional Eady waves. *Journal of the Atmospheric Sciences*, 46(19), 3055–3064.

Peixoto, P.S., Thuburn, J. & Bell, M.J. (2018) Numerical instabilities of spherical shallow-water models considering small equivalent depths. *Quarterly Journal of the Royal Meteorological Society*, 144(710), 156–171.

Ullrich, P.A., Jablonowski, C., Kent, J., Lauritzen, P.H., Nair, R.D. & Taylor, M.A. (2012) *Dynamical core model intercomparison project (DCMIP) test case document*, Vol. 83. Michigan: University of Michigan.

Ullrich, P., Reed, K. & Jablonowski, C. (2015) Analytical initial conditions and an analysis of baroclinic instability waves in f-and β-plane 3D channel models. *Quarterly Journal of the Royal Meteorological Society*, 141(693), 2972–2988.

Ullrich, P.A., Jablonowski, C., Kent, J., Lauritzen, P.H., Nair, R., Reed, K.A. et al. (2017) DCMIP2016: a review of non-hydrostatic dynamical core design and intercomparison of participating models. *Geoscientific Model Development*, 10(12), 4477–4509.

Visram, A. (2014) Asymptotic limit analysis for numerical models of atmospheric frontogenesis. PhD thesis, Imperial College London, 238.

Visram, A., Cotter, C. & Cullen, M. (2014) A framework for evaluating model error using asymptotic convergence in the Eady model. *Quarterly Journal of the Royal Meteorological Society*, 140(682), 1629–1639.

Williams, R. (1967) Atmospheric frontogenesis: a numerical experiment. *Journal of the Atmospheric Sciences*, 24(6), 627–641.

Williamson, D.L., Drake, J.B., Hack, J.J., Jakob, R. & Swarztrauber, P.N. (1992) A standard test set for numerical approximations to the shallow water equations in spherical geometry. *Journal of computational physics*, 102(1), 211–224.

Yamazaki, H., Shipton, J., Cullen, M.J., Mitchell, L. & Cotter, C.J. (2017) Vertical slice modelling of nonlinear eady waves using a compatible finite element method. *Journal of Computational Physics*, 343, 130–149.

Zarzycki, C.M., Jablonowski, C., Kent, J., Lauritzen, P.H., Nair, R., Reed, K.A. et al. (2019) DCMIP2016: the splitting supercell test case. *Geoscientific Model Development*, 12(3), 879–892.

How to cite this article: Yamazaki, H. & Cotter, C.J. (2025) A vertical-slice frontogenesis test case for compressible non-hydrostatic dynamical cores of atmospheric models. *Quarterly Journal of the Royal Meteorological Society*, 151:e5039. Available from: https://doi.org/10.1002/qj.5039

APPENDIX A. VARIATIONAL DERIVATION OF THE MODEL

In this Appendix we summarise briefly the variational derivation of the vertical-slice compressible Eady model, since it differs slightly from the model presented in section 5 of Cotter and Holm (2013), due to the modification to the Exner pressure. The Lagrangian for the system is

$$\ell[\boldsymbol{u}, v, D, \theta_S] = \int_\Omega \underbrace{\frac{D}{2}\left(|\boldsymbol{u}|^2 + v^2\right) + fDvx}_{\text{total kinetic energy}} - \underbrace{gDz}_{\text{gravitational potential energy}} - \underbrace{D\theta_S(c_v\Pi - c_p\Pi_0)}_{\text{internal energy}}\, dx\, dz, \tag{A1}$$

where θ_S is the in-slice temperature, transported according to

$$\frac{\partial \theta_S}{\partial t} + \boldsymbol{u}\cdot\nabla\theta_S + sv = 0, \tag{A2}$$

with the idea that the total potential temperature is $\theta \approx \theta_S + sy$ in the region of $y = 0$, where D is the in-slice density, transported according to

$$\frac{\partial D}{\partial t} + \nabla\cdot(\boldsymbol{u}D) = 0. \tag{A3}$$

Equation (A1) differs from the Lagrangian in Cotter and Holm (2013) by the inclusion of Π_0, a constant. Combining the two formulae in Equation (6) gives

$$\Pi = \left(\frac{DR\theta_S}{p_0}\right)^{\gamma-1}, \tag{A4}$$

where $\gamma = c_p/c_v$, and we have

$$\frac{\partial \Pi}{\partial \theta_S} = \frac{\gamma-1}{\theta_S}\Pi = \frac{R}{c_v\theta_S}\Pi, \qquad \frac{\partial \Pi}{\partial D} = \frac{R}{c_v D}\Pi. \tag{A5}$$

The functional derivatives are then

$$\frac{\delta \ell}{\delta \boldsymbol{u}_S} = D\boldsymbol{u}_S, \tag{A6}$$

$$\frac{\delta \ell}{\delta v} = D(v + fx), \tag{A7}$$

$$\frac{\delta \ell}{\delta D} = \frac{1}{2}(\|\boldsymbol{u}\|^2 + v^2) + fvx - gz - c_p\theta_S(\Pi - \Pi_0), \tag{A8}$$

$$\frac{\delta \ell}{\delta \theta_S} = c_p D(\Pi - \Pi_0). \tag{A9}$$

1477870x, 2025, 772, Downloaded from https://rmets.onlinelibrary.wiley.com/doi/10.1002/qj.5039 by Imperial College London, Wiley Online Library on [12/03/2026]. See the Terms and Conditions (https://onlinelibrary.wiley.com/terms-and-conditions) on Wiley Online Library for rules of use; OA articles are governed by the applicable Creative Commons License

Substitution into eq. 2.9 of Cotter and Holm (2013) then gives

$$\frac{\partial D\boldsymbol{u}}{\partial t} + \nabla\cdot(\boldsymbol{u}\otimes D\boldsymbol{u}) + (\nabla\boldsymbol{u})^{\mathrm{T}}\cdot D\boldsymbol{u} + D(v+fx)\nabla v - D\nabla\left(\frac{1}{2}(\|\boldsymbol{u}\|^2+v^2) + fvx - gz - c_{\mathrm{p}}\theta_S(\Pi-\Pi_0)\right) + c_{\mathrm{p}}D(\Pi-\Pi_0)\nabla\theta_S = 0, \tag{A10}$$

$$\frac{\partial D(v+fx)}{\partial t} + \nabla\cdot(\boldsymbol{u}D(v+fx)) + sc_{\mathrm{p}}D(\Pi-\Pi_0) = 0, \tag{A11}$$

and further manipulations in combination with Equations (A2) and (A3) lead to Equations (1–4), noting that $\nabla\Pi_0 = 0$ (because Π_0 is a constant).

Appendix B of Cotter and Holm (2013) derives the Lie–Poisson formulation for the vertical-slice framework, demonstrating a conserved energy/Hamiltonian given by

$$E = \int_\Omega \frac{\delta\ell}{\delta\boldsymbol{u}}\cdot\boldsymbol{u} + \frac{\delta\ell}{\delta v}v\,dx\,dz - \ell[\boldsymbol{u},v,\theta_S,D]. \tag{A12}$$

For ℓ from Equation (A1), this becomes

$$E = \int_\Omega \frac{D}{2}\left(|\boldsymbol{u}|^2+v^2\right) + gDz + D\theta_S(c_{\mathrm{v}}\Pi - c_{\mathrm{p}}\Pi_0)\,dx\,dz, \tag{A13}$$

which just corresponds to the (relative, that is, the Coriolis part is removed) kinetic energy plus the potential energy, as expected.

Finally, from eq. 2.11 of Cotter and Holm (2013) we have the vertical-slice Kelvin circulation theorem,

$$\frac{d}{d\,t}\oint_{C(t)}\left(s\frac{1}{D}\frac{\delta\ell}{\delta\boldsymbol{u}} - \frac{1}{D}\frac{\delta\ell}{\delta v}\nabla\theta_S\right)\cdot\,d(x,z) = 0, \tag{A14}$$

where $C(t)$ is a closed loop transported in the x–z plane by the in-slice velocity $\boldsymbol{u}$. For ℓ from Equation (A1), this becomes

$$\frac{d}{d\,t}\oint_{C(t)}(s\boldsymbol{u} - (v+fx)\nabla\theta_S)\cdot\,d(x,z) = 0. \tag{A15}$$

After application of Stokes' Theorem and consideration of arbitrary $C(t)$, we obtain the material conservation of potential vorticity q,

$$\frac{\partial q}{\partial t} + \boldsymbol{u}\cdot\nabla q = 0, \qquad q = \left[s\ \mathrm{curl}\,\boldsymbol{u} + \nabla\theta_S\times(\nabla v + f\hat{x})\right]\cdot\hat{y}\,d(x,z), \tag{A16}$$

where $\hat{x}$ and $\hat{y}$ are the unit vectors pointing in the x- and y- directions respectively.

1477870x, 2025, 772, Downloaded from https://rmets.onlinelibrary.wiley.com/doi/10.1002/qj.5039 by Imperial College London, Wiley Online Library on [12/03/2026]. See the Terms and Conditions (https://onlinelibrary.wiley.com/terms-and-conditions) on Wiley Online Library for rules of use; OA articles are governed by the applicable Creative Commons License